

OAFuser: Towards Omni-Aperture Fusion for Light Field Semantic Segmentation of Road Scenes

Fei Teng*, Jiaming Zhang*, Kunyu Peng, Kailun Yang[†], Yaonan Wang, and Rainer Stiefelhagen

Abstract—Light field cameras can provide rich angular and spatial information to enhance image semantic segmentation for scene understanding in the field of autonomous driving. However, the extensive angular information of light field cameras contains a large amount of redundant data, which is overwhelming for the limited hardware resource of intelligent vehicles. Besides, inappropriate compression leads to information corruption and data loss. To excavate representative information, we propose an *Omni-Aperture Fusion model (OAFuser)*, which leverages dense context from the central view and discovers the angular information from sub-aperture images to generate a semantically-consistent result. To avoid feature loss during network propagation and simultaneously streamline the redundant information from the light field camera, we present a simple yet very effective *Sub-Aperture Fusion Module (SAFM)* to embed sub-aperture images into angular features without any additional memory cost. Furthermore, to address the mismatched spatial information across viewpoints, we present *Center Angular Rectification Module (CARM)* realized feature resorting and prevent feature occlusion caused by asymmetric information. Our proposed OAFuser achieves state-of-the-art performance on the UrbanLF-Real and -Syn datasets and sets a new record of 84.93% in mIoU on the UrbanLF-Real Extended dataset, with a gain of +4.53%. The source code of OAFuser will be made publicly available at <https://github.com/FeiBryantkit/OAFuser>.

Index Terms—Semantic segmentation, light field, scene parsing, vision transformers, scene understanding.

I. INTRODUCTION

AUTONOMOUS driving and intelligent transportation systems heavily rely on computer vision tasks, especially image semantic segmentation, which can produce pixel-level prediction results and contribute to determining the category, shape, and position of objects [1], [2], [3], [4]. To effectively apply semantic segmentation and achieve autonomous driving in real-world scenarios, three key factors become crucial: *accuracy*. To enhance the accuracy, advanced models, such as ConvNets [5], [6] and MLP-based methods [7], and attention mechanism [8], [9], are introduced. Furthermore, different

This work was supported in part by the Ministry of Science, Research and the Arts of Baden-Württemberg (MWK) through the Cooperative Graduate School Accessibility through AI-based Assistive Technology (KATE) under Grant BW6-03, in part by the University of Excellence through the “KIT Future Fields” project, in part by the Helmholtz Association Initiative and Networking Fund on the HAICORE@KIT partition, and in part by Hangzhou SurImage Technology Company Ltd.

F. Teng, J. Zhang, K. Peng, and R. Stiefelhagen are with the Institute for Anthropomatics and Robotics, Karlsruhe Institute of Technology, 76131 Karlsruhe, Germany.

K. Yang and Y. Wang are with the School of Robotics and the National Engineering Research Center of Robot Visual Perception and Control Technology, Hunan University, Changsha 410082, China.

*Equal contribution.

[†]Corresponding author (E-Mail: kailun.yang@hnu.edu.cn.).

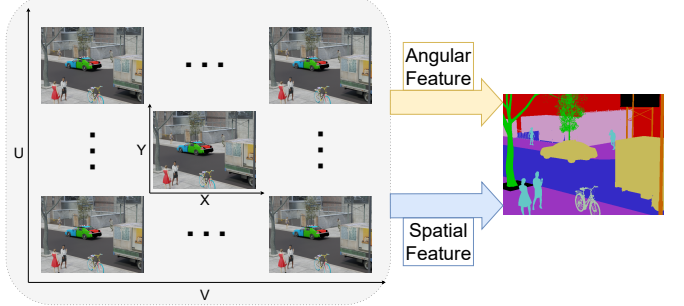


Fig. 1: A light field camera captures a more comprehensive range of spatial and angular information, which contribute to pixel-wise segmentation works. The fusion of omni-aperture features enhances urban semantic scene understanding.

fusion strategies for segmentation [10], [11], [12], [13] are proposed to improve the perception ability.

In this work, we explore the light field (LF) camera, which can capture both spatial and angular information of the driving scene, making it beneficial for autonomous driving. Specifically, due to the design of a micro-lens array and image sensor, light field cameras can simultaneously capture spatial information from different directions, yielding visual variations between the central and sub-aperture images. This novel mechanism can be utilized to distinguish those geometrically complex regions. Despite the theoretical benefits, we observe two under-explored challenges of applying LF cameras in semantic segmentation, as presented in Table I: (1) high demands on hardware and data processing; (2) effective use of angular features. In this work, we propose a novel **Omni-Aperture Fusion (OAFuser)** model, with the aim of addressing the aforementioned two challenges.

First, high memory cost for redundant sub-aperture and extra efforts related to complex data pre-processing is required to handle LF-based semantic segmentation. For example, assigning a feature extractor to each LF image can over-burden the device. The macro-pixel representation in the form of high-resolution images [14], [15] imposes also significant pressure on device capacity. Especially, using an LF camera with a spatial resolution of 640×480 and angular resolution of 9×9 will bring a macro-pixel image with 4320×5760 , imposing 81 times of data stream along the network module. However, compressing LF images into a depth map [16], [17] will additionally increase the complexity of the model. Moreover, the quality of generated depth map [18], [19] directly impacts the performance of segmentation. To overcome these issues and

Method	Hardware Demand and Extra Efforts			The Capacity of the Network		
	#Modality	Memory Cost	Independent of Depth Map	Angular Information	Feature Rectification	Independent of Image Quality
RGB Based Network	1	n.a.	n.a.	✗	✗	✗
RGB-D based Network	2	n.a.	✗	✗	✓	✗
OCR-LF [17]	More than 2	✗	✓	✓	✗	✗
PSPNet-LF [17]	More than 2	✗	✓	✓	✗	✗
LF-IENet [20]	More than 2	✗	Explicit	Implicit	✗	✗
OAFuser (ours)	Flexible	✓	✓	✓	✓	✓

TABLE I: Challenges of light field semantic segmentation. The *#Modality* indicates the number of sub-aperture images used. In the *Memory Cost*, *n.a.* denotes that the memory cost also increases with an increase in the number of images. *Independent of Depth Map* indicates whether depth information is required. *Angular Information* column describes the utilization of angular information. Finally, the *Independent of Image Quality* indicates the issue of out-of-focused images from light field cameras. As for LF-IENet, *Disparity Map* is explicitly generated, and *Angular Information* is hidden in the implicit branch.

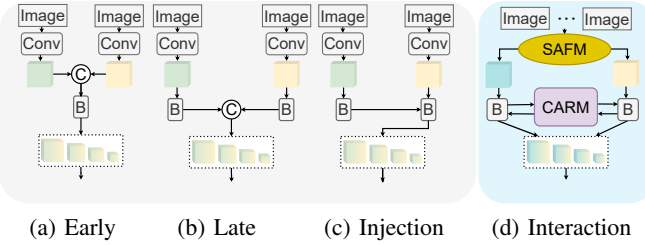


Fig. 2: **Paradigms of light field semantic segmentation model.** Compared to conventional fusion methods, our interaction fusion can handle an arbitrary number of LF images, and the features from different branches interact with each other.

explore the efficiency of using LF cameras without the need for additional hardware or architectural modifications, we propose a simple yet effective **Sub-Aperture Fusion Module (SAFM)** that allows our OAFuser network to utilize an arbitrary number of sub-aperture images, so as to achieve efficient semantic segmentation without additional memory cost. Especially, the SAFM can first distinguish the primary and interfering features channel-wise by analyzing the image features from different view directions. Besides, rich information from LF images is embedded into angular feature maps and spatial feature maps and further fed into respective transformer blocks. Thanks to the SAFM module, our OAFuser network can achieve better performance while avoiding excessive memory costs, which is crucial for autonomous driving applications.

Second, the ability of the network is regarding the performance, *i.e.*, angular feature expression and asymmetric feature rectification. Previous methods introduce a sub-optimal solution for the light field image representation. While stacking images into an array [17], [19] contains solely one-dimensional angular information, converting into a video sequence [21], [22] ignores the implicit relationship. Besides, direct merging images or features results in blurred or mixed boundaries, and this phenomenon is particularly severe with the increase of sub-aperture images since the images are captured from different viewpoints. Moreover, the images captured by the plenoptic camera [23], [24] contain much noise, and the initial light field images are not entirely focused, which can further exacerbate this issue. In this work, we introduce a **Center Angular Rectification Module (CARM)** to perform effective

rectification between the center view and the aperture-based features. Apart from other strategies in which the features are directly fused with others, our network adopts iteration feature rectification to incorporate the asymmetric angular feature and spatial features from the SAFM before the fusion stage, as shown in Fig. 2. This design allows our OAFuser network to explore the relationship between different features and has realigned the angular and spatial information, further boosting the segmentation task for road scene understanding.

To demonstrate the effectiveness of the proposed OAFuser architecture, we conduct a comprehensive variety of experiments on different light field semantic segmentation datasets. On the UrbanLF-Real dataset, OAFuser achieves 82.69% in mIoU with an increase of +3.37%. On the UrbanLF-Syn dataset, OAFuser surpasses previous works and attains 81.93% in mIoU. Compared to previous state-of-the-art methods, OAFuser reaches the best mIoU of 84.93% with a notable mIoU improvement of +4.53% on the UrbanLF-RealE dataset, while no additional parameters are required.

At a glance, we deliver the following contributions:

- We propose a novel Omni-Aperture Fusion model, *i.e.*, **OAFuser**, to perform light-field semantic segmentation with the arbitrary number of sub-aperture images.
- We design a **Sub-Aperture Fusion Module (SAFM)** to fuse and embed rich angular information from highly redundant representation, and a **Center Angular Rectification Module (CARM)** to match and rectify information imbalances caused by variations from different angles.
- We verify our method through extensive experiments on three datasets, *i.e.*, UrbanLF-Real, UrbanLF-Syn, and UrbanLF-RealE, which is a real-world dataset with extended synthetic samples.

II. RELATED WORK

In this section, the overview of semantic segmentation is introduced in Sec. II-A. Since the asymmetric feature representation from the light field camera, various multimodal semantic segmentation works are presented in Sec. II-B. Furthermore, to boost the angular information expression of light field cameras, several applications in other areas are also introduced in Sec. II-C

A. Semantic Segmentation

Semantic scene segmentation, as a fundamental task of computer vision, plays a crucial role in scene understanding tasks, such as autonomous driving and intelligent transportation systems [1], [25], by assigning a category to each pixel. Since FCN [26] pioneers the use of convolutional neural networks to replace fully connected networks to propose an end-to-end framework, many segmentation works have emerged based on this approach, and the efficiency and accuracy of segmentation have been largely improved. For instance, [27], [28] adopt an encoder-decoder structure to capture contextual information and local details. Then, [27], [29] introduce dilated convolution to increase the receptive field. To enhance the global context representation, [30], [31] adopt a pyramidal hierarchy in the encoding path. Furthermore, enhancing prior contextual information [32], [33], [34] contributes to improving segmentation results. Since the introduction of the self-attention mechanism in vision tasks [35], many following works [8], [9], [25] propose dense prediction, attention-based models. Meanwhile, some other works introduce lightweight backbones to speed up the inference [36], [37], [38].

Although those works demonstrate excellent results in handling dense prediction tasks, they still suffer from the limitation of image quality and lead to performance degeneration in handling complete areas, such as shallow or out-of-focus areas in real-world self-driving scene understanding scenarios.

B. Multi-Modal Semantic Segmentation

The multiple sub-aperture images captured by the light field camera can be considered as various RGB modalities with inherent relationships. Therefore, the research on multi-modal semantic segmentation is essential for exploring the potential of light field cameras. ACNet [39] and EDCNet [40] leverage attention connections for facilitating cross-modal interactions in RGB-Depth and RGB-Event semantic segmentation, respectively. MMFNet [41] enables the fusion of multiple medical images through the aggregation of different features in spatial and channel domains. NestedFormer [42] proposed a feature aggregation module to fulfill multimodal medical image segmentation. Furthermore, ESA-Net [43] and SA-Gate [16] utilize depth maps and RGB images to achieve high-accuracy semantic segmentation by employing uniquely designed fusion modules. PGSNet [44], which introduces a dynamic integration module, achieves glass segmentation. Additionally, [45], [46], [47] adopt RGB-thermal image fusion. Especially, the works of CMX [13], [48] present an arbitrary-modal fusion network, which can handle RGB and any other modality, such as depth, thermal, polarization, event, or LiDAR data. HRFuser [49] realizes the fusion of an arbitrary number of additional modalities as supplementary information into RGB images by introducing multi-window cross-attention.

Different from these methods, which are focused on handling symmetrical modalities, our proposed OAFuser focuses on the utilization of the angular information diversity in light-field images and considers the mismatching from images captured by all sub-apertures of light-field cameras.

C. Light Field Scene Understanding

While light-field cameras are still under-explored in semantic segmentation, they have found wide applications in various areas, such as saliency detection [50], [51], depth estimation [52], [53], and super-resolution [54], [55], due to their rich visual information. Several works have leveraged the potential of light-field cameras. FES [56] achieves sub-aperture feature fusion via spatial and channel attention. NoiseLF [57] utilizes the all-focus central-view image and its corresponding focal stack, with a unique-designed forgetting matrix and confidence re-weighting strategy, to achieve supervised saliency detection under noisy labels.

Furthermore, several works [58], [59], [60] employ sub-aperture images, macro-pixel images, epipolar images, or a combination of some of those images to generate high-resolution light field images. Moreover, AIFLFNet [61] utilized light field images to estimate depth information. Additionally, SAA-Net [62] introduces spatial-angular attention modules for light field image reconstruction. Especially, a design from [14] proposes a unified block for handling macro-pixel images, which can be used for both super-resolution and disparity estimation. For light-field semantic segmentation, the work of [17] utilizes stacks of sub-aperture images from certain directions achieving the segmentation of central-view images. LFIE-Net [20] introduces an explicit branch to generate disparity maps within the network and cooperates with the sub-aperture images to achieve dense semantic segmentation.

Unlike existing works which are limited by memory costs when processing light-field images, our proposed OAFuser has the capability to handle an arbitrary number of sub-aperture images without parameter demands for light-field road-scene semantic understanding.

III. METHODOLOGY

This section provides a detailed introduction to our proposed network, *i.e.*, *Omni-Aperture Fuser (OAFuser)*, which is tailored for light field semantic segmentation. The overall OAFuser architecture is presented in Sec. III-A. The *Sub-Aperture Fusion Module (SAFM)* for light-field feature aggregation is introduced in Sec. III-B. The *Center Aperture Rectification Module (CARM)* is in Sec. III-C.

A. Proposed OAFuser Architecture

As shown in Fig. 3, the proposed OAFuser is constructed with a four-stage encoder and a decoder. The encoder consists of the proposed SAFM and CARM to handle the feature fusion, feature embedding, and feature rectification, respectively. For simplicity, the following description is based on stage one, which is the same for the other three stages. Especially, the arbitrary number of light field images is described as sub-aperture images $F_{s_i} \in \mathbb{R}^{H \times W \times 3}$ and central view image $F_c \in \mathbb{R}^{H \times W \times 3}$, where s_i is the i -th sub-aperture image in range $[1, N]$. All of them are fed into SAFM to embed angular feature $F_{agl} \in \mathbb{R}^{\frac{H}{8} \times \frac{W}{8} \times 64}$ that contains rich angular information and spatial feature $F_{spl} \in \mathbb{R}^{\frac{H}{8} \times \frac{W}{8} \times 64}$ which focus on spatial information for the central view. By applying two different

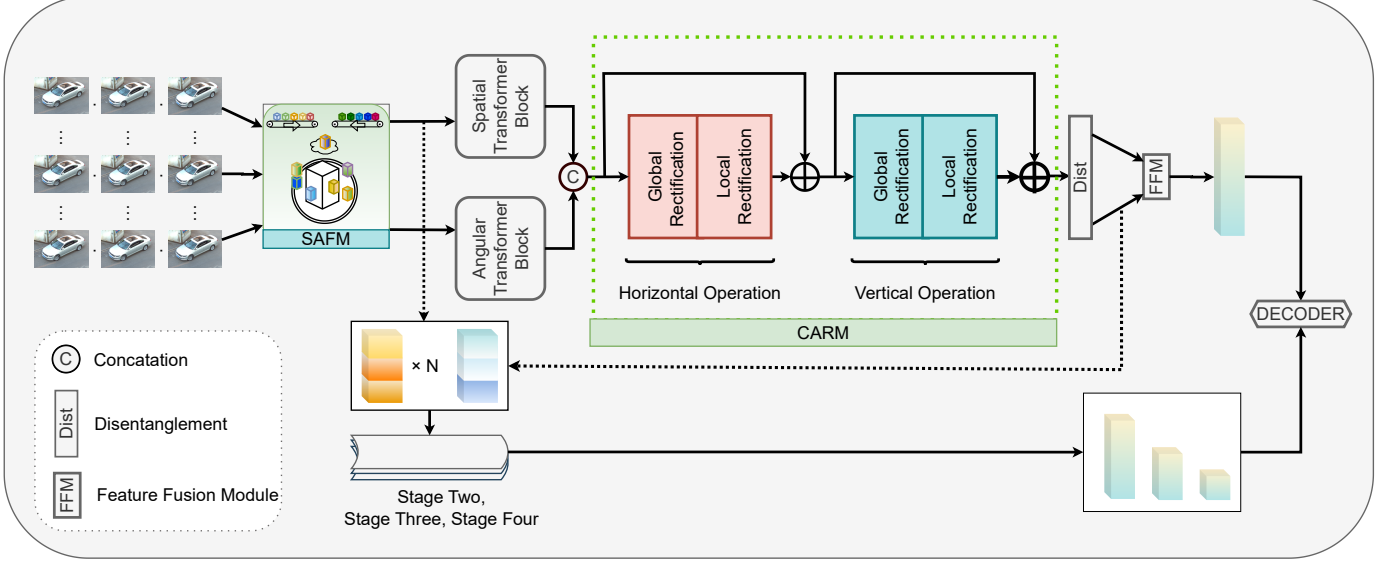


Fig. 3: **Overall structure of the OAFuser model for omni-aperture fusion.** An arbitrary number of sub-aperture images is fed into the model. The *Sub-Aperture Fusion Module* (SAFM) in Sec. III-B generates both angular feature and spatial feature. The *Horizontal Operation* and *Vertical Operation* of *Center Aperture Rectification Module* (CARM) in Sec. III-C are implemented for asymmetric feature rectification. Afterward, the four-stage features are fed into *Decoder* for final semantic segmentation.

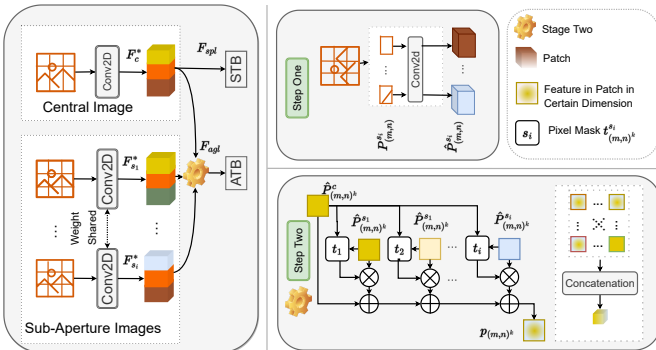


Fig. 4: **The structure of the Sub-Aperture Fusion Module (SAFM).** It consists of two stages. Given $N + 1$ images, which include N sub-aperture images and one central view image, are conducted in SAFM. SAFM embeds the rich information into angular feature F_{agl} and Spatial Feature F_{spl} . *STB* and *ATB* denote Spatial Transformer Block and Angular Transformer Block respectively.

transformer blocks following [13], both of the features transformed into $F_{agl}^* \in \mathbb{R}^{\frac{H}{8} \times \frac{W}{8} \times 64}$ and $F_{spl}^* \in \mathbb{R}^{\frac{H}{8} \times \frac{W}{8} \times 64}$. After that, the angular and spatial features are concatenated for the next CARM, which includes Horizontal Operation and Vertical Operation for feature rectification along the horizon and vertical direction to eliminate asymmetry. Specially, the concatenation of F_{spl}^* and F_{agl}^* along the horizon direction is applied to obtain $F_{c1} \in \mathbb{R}^{\frac{H}{8} \times \frac{W}{4} \times 64}$. After the Global Rectification and Local Rectification, the horizontally rectified feature $F^H \in \mathbb{R}^{2 \times \frac{H}{8} \times \frac{W}{8} \times 64}$ is obtained. Then, given the feature F^H , the feature $F_{c2} \in \mathbb{R}^{\frac{H}{4} \times \frac{W}{8} \times 64}$ is obtained by the operation of disentanglement and concatenation along the vertical direction. Especially, $F^H \in \mathbb{R}^{2 \times \frac{H}{8} \times \frac{W}{8} \times 64}$ is dis-

entangled into $F_{agl}^H \in \mathbb{R}^{\frac{H}{8} \times \frac{W}{8} \times 64}$ and $F_{spl}^H \in \mathbb{R}^{\frac{H}{8} \times \frac{W}{8} \times 64}$. F_{agl}^H and F_{spl}^H are further concatenated along vertical direction. After applying Global Rectification and Local Rectification in Vertical Operation, the rectified features $F^G \in \mathbb{R}^{2 \times \frac{H}{8} \times \frac{W}{8} \times 64}$. $F_{agl}^G \in \mathbb{R}^{\frac{H}{8} \times \frac{W}{8} \times 64}$ and $F_{spl}^G \in \mathbb{R}^{\frac{H}{8} \times \frac{W}{8} \times 64}$ is obtained by disentanglement of F^G . Furthermore, those two rectified features, *i.e.*, F_{agl}^G and F_{spl}^G are fused by using the FFM module [13], which integrates two different features, to produce the final feature f_1 for this stage. The weights between Horizontal Operation and Vertical Operation are shared.

Note that one of our crucial designs is *all sub-aperture information is fed into each stage*, which allows our network to consider all the sub-aperture images throughout the whole process effectively. The pyramidal features f_1, f_2, f_3, f_4 are obtained via the four-stage encoder in a dimension of $\{64, 128, 320, 512\}$. Afterward, the multi-stage features are further fed into MLP Decoder [8] for final prediction.

B. Sub-Aperture Fusion Module

To retrieve the rich angular and spatial information from light field images, we introduce the SAFM module, which embeds that information into angular features and spatial features. As shown in Fig. 4, the SAFM consists of two steps. The first step of our SAFM is to extract features from all the light field images. All images are firstly divided into patches $P_{(m,n)}^s$, $P_{(m,n)}^c$, corresponding to sub-aperture images F_{s_i} and F_c , and further fed into the convolutional layer to extract features, resulting in $\hat{P}_{(m,n)}^s$ and $\hat{P}_{(m,n)}^c$, where m, n denotes the relative position of the patch in a single feature map. The patch size follows [13]. Especially our work aims to segment the central view image. Thus, the weights for the center view are performed individually, which ensures the spatial information of the central view remains independent. The

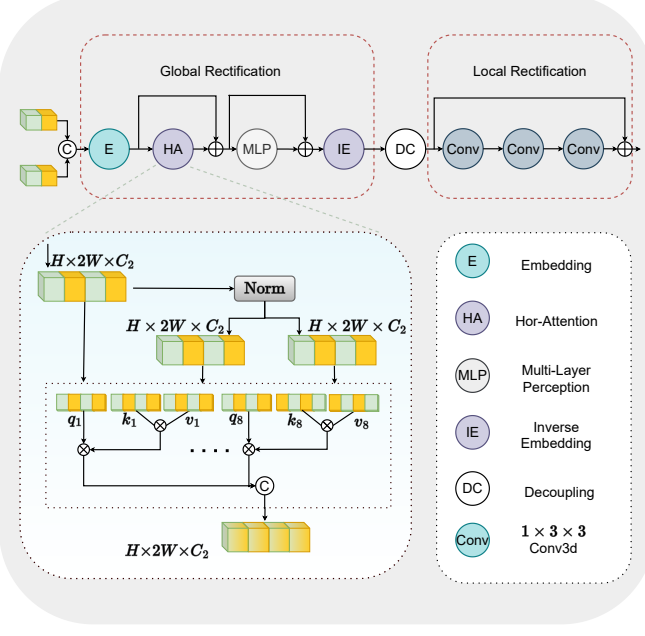


Fig. 5: **The structure of Horizontal Operation in Center Angular Rectification Module (CARM).** It consists of Global Operation and Local Operation.

weights for sub-aperture images are shared between different sub-aperture images. The calculations are presented in Eq. (1) and Eq. (2):

$$\hat{P}_{(m,n)}^{s_i} = \text{Conv}^{\text{sub}}(C_{\text{in}}, C_{\text{out}})(P_{(m,n)}^{s_i}), \quad (1)$$

$$\hat{P}_{(m,n)}^c = \text{Conv}^{\text{cen}}(C_{\text{in}}, C_{\text{out}})(P_{(m,n)}^c), \quad (2)$$

where $\text{Conv}(C_{\text{in}}, C_{\text{out}})$ means the convolutional layer with input dimension C_{in} and output dimension C_{out} . For the first stage, C_{in} is 3 and C_{out} is 64. After that, the central image features F_{spl} are obtained by combining different patches $\hat{P}_{(m,n)}^c$ and fed into the Spatial Transformer Block (STB). Meanwhile, the patches of the central view are also fed into the next step to cooperate with patches of the sub-aperture image to obtain angular features.

Afterward, the second step of SAFM is illustrated in Fig. 4, which is presented as the yellow gear symbol. For each patch $\hat{P}_{(m,n)}^{s_i}$ of dimension k , the channel score $e_{(m,n)}^{s_i}$ is calculated by obtaining the euclidean distance between each patch from the sub-aperture feature in dimension k and the corresponding patch from center view feature in dimension k , as in Eq. (3):

$$e_{(m,n)}^{s_i} = \text{Abs}(\hat{P}_{(m,n)}^c - \hat{P}_{(m,n)}^{s_i}), \quad (3)$$

where $\text{Abs}(\cdot)$ denotes absolute value between two patch in channel k . Given the $e_{(m,n)}^{s_i}$, the mask score $t_{(m,n)}^{s_i}$ for $\hat{P}_{(m,n)}^{s_i}$ is obtained by mapping into the range of [1,0] and squaring them to enhance the discrimination, as shown in Eq. (4).

$$t_{(m,n)}^{s_i} = (\Theta\{e_{(m,n)}^{s_i}\})^2, \quad (4)$$

where $\Theta\{\cdot\}$ denotes mapping operation. After obtaining the mask scores, the certain patch $P_{(m,n)}^k$ of angular feature

can be calculated. To be more detailed, the patch $P_{(m,n)}^k$ in angular feature F_{agl} at position (m, n) in channel k can be calculated by summarizing the corresponding central view patch $\hat{P}_{(m,n)}^c$ with masked sub-aperture patches $\hat{P}_{(m,n)}^{s_i}$, as in Eq. (5).

$$P_{(m,n)}^k = \hat{P}_{(m,n)}^c + \sum_{i=1}^N t_{(m,n)}^{s_i} \cdot \hat{P}_{(m,n)}^{s_i}. \quad (5)$$

Finally, the patch of angular feature $P_{(m,n)}$ is obtained by concatenation of $P_{(m,n)}^k$ as in Eq. (6). The angular feature F_{agl} is filled by $P_{(m,n)}$ and further fed into Angular Transformer Block (AFB).

$$P_{(m,n)} = \text{Concat}(P_{(m,n)}^k). \quad (6)$$

C. Central Angular Rectification Module

To eliminate information asymmetry, the CARM is a crucial design to achieve rectification of spatial and angular features and meanwhile rearrange the feature captured by different viewpoints. As shown in Fig. 5, two features from different transformer blocks are fed into CARM, which includes Horizontal Operation and Vertical Operation. Since Horizontal Operation and Vertical Operation are symmetric, only Horizontal Operation is introduced in detail. In each operation, Global Rectification and Local Rectification are applied to rectify feature cues in different regions. At the end of CARM, the two features F_{agl}^G and F_{spl}^G , which correspond to F_{agl}^* and F_{spl}^* , are further fed into FFM (Feature Fusion Module).

Specifically, in the Horizontal Operation, F_{agl}^* and F_{spl}^* is first concatenated along horizontal direction into feature $F_{c1} \in \mathbb{R}^{\frac{H}{8}H \times \frac{W}{4} \times 64}$. To intuitive represents the dimension change between different steps, we use $F_{c1} \in \mathbb{R}^{H \times 2W \times C_1}$ as the concatenated feature. F_{c1} is firstly fed into the **Global Rectification** stage. By applying an embedding process, F_{c1} is projected into $F_{c1}^* \in \mathbb{R}^{H \times 2W \times C_2}$, which contain a set of tokens $T_{c1}^* \in \mathbb{R}^{2W \times C_2}$, with the projection matrix $M_{in} \in \mathbb{R}^{C_1 \times C_2}$, where C_1 denotes the input dimension of features, and C_2 denotes the embedding dimension for each token, the number of tokens is $2W$. To mitigate the covariate shift, $\hat{F}_{c1}^* \in \mathbb{R}^{H \times 2W \times C_2}$ with tokens $\hat{T}_{c1}^* \in \mathbb{R}^{2W \times C_2}$ is obtained by applying normalization of F_{c1}^* , following [35]. Then, the tokens, which represent the feature cues in a row, are utilized to generate query (Q), key (K), and value (V). To be more specific, $Q \in \mathbb{R}^{2W \times C_2}$ and $K \in \mathbb{R}^{2W \times C_2}$ are obtained by multiplication of tokens \hat{T}_{c1}^* with matrices $M_q \in \mathbb{R}^{C_2 \times C_2}$ and $M_k \in \mathbb{R}^{C_2 \times C_2}$, respectively. The matrix $M_v \in \mathbb{R}^{C_2 \times C_2}$ multiplies the T_{c1}^* to generate $V \in \mathbb{R}^{2W \times C_2}$. Furthermore, Q , K , and V are divided along the channel dimension and fed into eight heads. The similarity of each head can be calculated by dot product and followed by a Softmax function to obtain the similarity scores in each head between those tokens, as in Eq. (7).

$$\text{Similarity}_{\text{head}_i} = \text{Softmax} \frac{Q_i \cdot K_i^T}{\sqrt{D_i}}, \quad i \in [1, 8]. \quad (7)$$

Dataset	Train	Val	Test	Total
UrbanLF-Real	580	80	164	824
UrbanLF-Syn	172	28	50	250
UrbanLF-RealE	780	80	164	1024

TABLE II: **Statistic information of light field semantic segmentation datasets.** UrbanLF-RealE denotes UrbanLF-Real with an extension of synthetic samples for training.

Based on the similarity scores, the rectified tokens $T_{h_i}^a$ in each head can be obtained by multiplying with V_i , as in Eq. (8).

$$T_{h_i}^a = \text{Similarity}_{head_i} \cdot V_i, \quad i \in [1, 8]. \quad (8)$$

The final tokens $T_h^a \in \mathbb{R}^{2W \times C_2}$ are obtained by concatenation, as in Eq. (9).

$$T_h^a = \text{Concat}\{T_{h_1}^a, T_{h_2}^a, \dots, T_{h_8}^a\}. \quad (9)$$

Given the final tokens T_h^a , an MLP layer is adapted, and a linear layer is to project tokens into demotion C_1 . The final feature $\bar{F}_h^a \in \mathbb{R}^{H \times 2W \times C_1}$ after Global Rectification can be formulated as in the Eq. (10),

$$\bar{F}_h^a = \text{LN}(C_2, C_1)(\text{MLP}(F_h^a) + F_h^a), \quad (10)$$

where $\text{LN}(C_2, C_1)(\cdot)$ denotes linear projection.

By decoupling the feature \bar{F}_h^a , the rectified feature stack $F_h^l \in \mathbb{R}^{2 \times H \times W \times C_1}$ is obtained. Furthermore, to further rectify the features in surrounding areas, the **Local Rectification** stage, which contains three convolutional layers, is implemented as in Eq. (12), where C denotes the input channel and output channel, $\{\cdot\} \otimes 2$ denotes repeat those layers two times.

$$\hat{F}_h^l = \{LReLU(\text{Conv3D}(C, C)(F_h^l))\} \otimes 2, \quad (11)$$

$$F^H = \text{Conv3D}(C, C)(\hat{F}_h^l). \quad (12)$$

By disentangling of $F^H \in \mathbb{R}^{2 \times H \times W \times C_1}$, $F_{agl}^H \in \mathbb{R}^{H \times W \times C_1}$ and $F_{spl}^H \in \mathbb{R}^{H \times W \times C_1}$ is obtained and further fed into Vertical Operation after concatenation.

IV. EXPERIMENT RESULTS

A. Datasets

Our experiments are based on the UrbanLF dataset [17]. The dataset comprises 14 categories for urban semantic scene

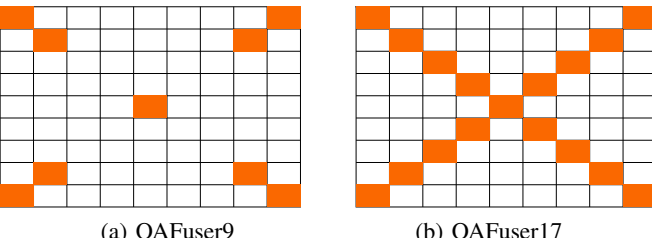


Fig. 6: **The proposed selection strategy** of light field images, i.e., OAFuser9 (left) and OAFuser17 (right).

Method	Type	Acc (%)	mAcc (%)	mIoU (%)
PSPNet [63]	RGB	91.21	83.87	76.34
DeepLabv3+ [27]	RGB	91.02	83.53	76.27
SETR [64]	RGB	92.16	84.27	77.74
OCR [65]	RGB	92.02	85.17	78.60
Accel [66]	Video	89.15	80.69	71.64
TDNet [67]	Video	91.05	83.38	76.48
DAVSS [21]	Video	91.04	83.54	75.91
TMANet [22]	Video	91.67	84.13	77.14
PSPNet-LF [17]	LF	92.14	84.86	78.10
OCR-LF [17]	LF	92.51	86.31	79.32
LF-IENet ⁴ [20]	LF	92.01	85.10	78.09
LF-IENet ³ [20]	LF	92.09	86.03	79.19
OAFuser9	LF	94.45 (+1.94)	88.21 (+1.90)	82.69 (+3.37)
OAFuser17	LF	94.08 (+1.52)	87.74 (+1.43)	82.21 (+2.89)

TABLE III: Quantitative results on the UrbanLF-Real dataset. Acc (%), mAcc (%), and mIoU (%) are reported. The best results are highlighted in red. The variation term indicates the performance difference from the previous best result.

understanding. Each sample in the dataset consists of 81 sub-aperture images with an angular resolution of 9×9 . In our experiments, we follow the protocols proposed in UrbanLF and conducted three sets of experiments: Urban-Syn, Urban-Real, and UrbanLF-RealE. The UrbanLF-RealE is an extension of all real and synthetic data. Table II presents the number of images used for training, evaluation, and testing.

B. Implementation Details

The image size for UrbanLF-Syn is 640×480 while applying zero padding converts samples in UrbanLF-Real into a size of 640×480 . Data augmentation is applied with random flipping with a probability of 0.5, random scaling factors $\{0.5, 0.75, 1, 1.25, 1.5, 1.75\}$, normalization with mean factors $\{0.485, 0.456, 0.406\}$, and standard deviation factors $\{0.229, 0.224, 0.225\}$. We use the AdamW optimizer with momentum parameters $\{0.9, 0.999\}$ and a weight decay of 0.01. The original learning rate is set to $6e^{-5}$ and scheduled using the polynomial strategy with a power of 0.9. The first 10 epochs are used to warm up the models.

For experiments on the three different datasets, the training process adapts on three A40 GPUs with a batch size of 3 on each GPU and the number of training epochs is limited to a maximum of 500, and the model is based on the MiT-B4 per-train weight [8]. For the ablation study of architecture, we train our model with MiT-B2 [8] on one A5000 GPU with a batch size of 2 and epoch 200. With the MiT-B0 [8] on one A5000 GPU with a batch size of 2, we conduct an ablation study on the CARM and the investigation on the selection of sub-aperture images. For the selection of sub-aperture images, we choose images that are rich in angular information, mostly in the diagonal, as shown in Fig. 6. The experiments on the selection strategy of sub-aperture light-field images are discussed in Sec. V-E.

Method	Type	Acc (%)	mAcc (%)	mIoU (%)
PSPNet [63]	RGB	89.39	84.48	75.78
SETR [64]	RGB	90.97	85.26	77.69
DeepLabv3+ [27]	RGB	89.60	83.55	75.39
OCR [65]	RGB	91.50	86.96	79.36
ACNet [39]	RGB-D	92.53	86.62	78.56
MTINet [5]	RGB-D	91.24	86.94	79.10
ESANet [43]	RGB-D	91.81	86.26	79.43
SA-Gate [16]	RGB-D	92.10	87.04	79.53
Accel [66]	Video	87.56	80.52	70.48
TDNet [67]	Video	89.06	83.43	74.71
DAVSS [21]	Video	89.47	82.94	74.27
TMANet [22]	Video	89.76	84.44	76.41
PSPNet-LF [17]	LF	90.55	85.91	77.88
OCR-LF [17]	LF	92.01	87.71	80.43
LF-IENet ⁴ [20]	LF	90.42	86.17	78.27
LF-IENet ³ [20]	LF	92.41	88.31	81.78
OAFuser9	LF	93.23 (+0.82)	88.26 (-0.05)	81.64 (-0.14)
OAFuser17	LF	93.42 (+1.01)	88.22 (-0.09)	81.93 (+0.15)

TABLE IV: Quantitative results on the UrbanLF-Syn dataset. Acc (%), mAcc (%), and mIoU (%) are reported. The best results are highlighted in red. The variation term indicates the performance difference from the previous best result.

C. Quantitative Results

To verify our methods, we compare OAFuser with other methods, which include RGB-based methods [27], [63], [64], [65], video-based light field semantic segmentation methods [21], [22], [66], [67], and several specific designs for light field semantic segmentation [17], [20] on three datasets, *i.e.*, UrbanLF-Real, UrbanLF-Syn, UrbanLF-RealE.

1) Results on UrbanLF-Real:

Table III presents the quantitative results on the UrbanLF-Real dataset, which is challenging due to issues like out-of-focus from the plenoptic camera and remaining consistency with light field camera implementation without further data pre-processing in real-world scenarios. Our OAFuser9 model achieves a state-of-the-art mIoU score of 82.69%, showing an improvement of 3.37% compared to previous methods. Similarly, our OAFuser17 model achieves a mIoU of 82.21%, with an increase of 2.89%. Regarding Acc and mAcc, both our OAFuser9 and OAFuser17 have improved by over 1% compared to previous works. The small performance gap between our OAFuser9 and OAFuser17 is attributed to the image quality, which will be discussed in Sec. V-C.

As we increase the number of sub-aperture images, we also observe a corresponding increase in the presence of irrelevant features. Furthermore, the abundance of out-of-focus and blurry images has led to inaccurate guidance, which surprisingly benefits our network. From another perspective, it also demonstrates the necessity of our correction module in handling semantic segmentation with light field cameras. The results clearly demonstrate the remarkable effectiveness of the suggested module structure and support our proposed approach, which leverages the rich angular information present

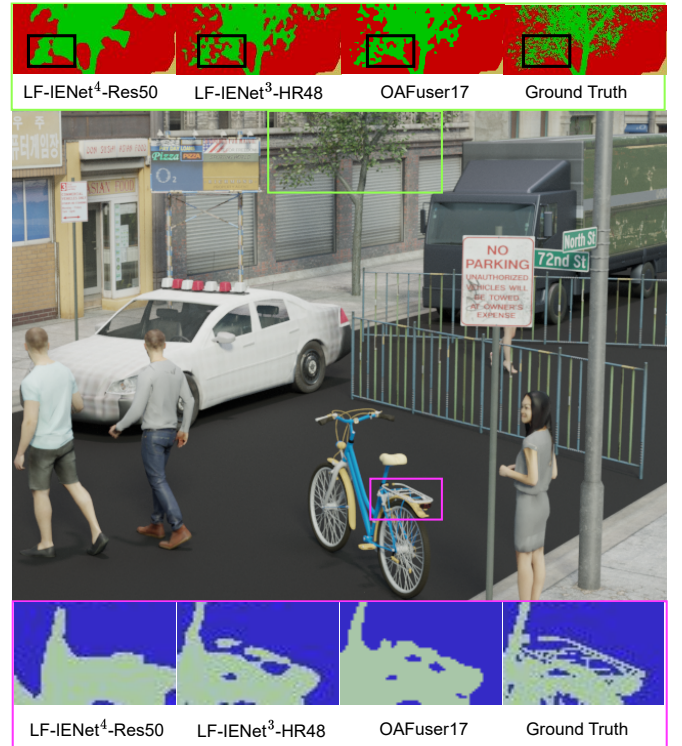


Fig. 7: Qualitative result for our network on the UrbanLF Syn dataset compared with LF-IENet [20].

in sub-aperture images and combines it with the spatial information from the central view. This fusion of data proves to be beneficial for accurately segmenting the central view image.

2) Results on UrbanLF-Syn:

The quantitative results on the synthetic dataset are shown in Table IV. Among all the models assessed, OAFuser17 attains the highest mIoU. Comparatively, OAFuser9 exhibits slightly inferior performance to LF-IENet³. This discrepancy in performance can be primarily attributed to the restricted size of the synthetic dataset, encompassing merely 173 samples for training purposes. In concrete terms, OAFuser makes use of the small differences present among different sub-aperture images to capture intricate angular details. These details are then combined with the appropriate spatial information obtained from the main viewpoint. This approach differs from previous methods that mainly focus on spatial information limited to the central view and overlook the angular information available from the light field camera. Additionally, a key feature of OAFuser is its ability to eliminate the need for pre-processing of initial light field images, showcasing its capability to handle raw light field data by effectively utilizing various angular information. Importantly, when using fully focused images from synthetic datasets, the network's processing capabilities are not adequately demonstrated. Furthermore, it can be clearly seen from Fig. 7 in areas of complex structures, such as the leaves and bicycle pillion seats. Compared with LF-IENet, which leads to loss of global context for objects, such as the gaps between objects and their connection with branches being disrupted, our approach demonstrates better segmentation results even with 17 sub-aperture images. This

Method	Type	Acc (%)	mAcc (%)	mIoU (%)
PSPNet [63]	RGB	91.73	84.47	77.71
DeepabV3 ⁺ [27]	RGB	91.33	83.86	76.70
SETR [64]	RGB	92.72	85.55	79.06
OCR [65]	RGB	92.56	86.56	79.90
Accel [66]	Video	89.40	82.30	72.85
TDNet [67]	Video	91.48	84.25	77.52
DAVSS [21]	Video	91.96	85.21	77.31
TMANet [22]	Video	91.84	84.81	78.13
PSPNet-LF [17]	LF	92.69	86.01	79.45
OCR-LF [17]	LF	92.95	86.94	80.40
OAFuser9	LF	94.61 (+1.66)	89.84 (+2.90)	84.93 (+4.53)
OAFuser17	LF	93.74 (+0.79)	88.92 (+1.98)	82.42 (+2.02)

TABLE V: Quantitative results on the UrbanLF-RealE dataset. Acc (%), mAcc (%), and mIoU (%) are reported. The best results are highlighted in red. The variation term indicates the performance difference from the previous best result.

means the excellent performance of our network to utilize sub-aperture images and, by rectification, OAFuser remains consistent with the information captured from different points of view. This claim has been also supported by thorough experiments conducted on both the UrbanLF-Real dataset and the UrbanLF-RealE dataset.

3) Results on UrbanLF-RealE:

UrbanLF-RealE, which involves not only real-world samples but also extends to multiple synthetic samples, poses significant challenges to the performance of the model. This complex combination of data is more aligned with unconstrained scenarios. As shown in Table V, OAFuser achieves state-of-the-art performance with mIoU of 84.93%. The result exceeds all the existing methods by more than 4.53%. The accuracy of OAFuser17 decreases compared to OAFuser9, which is caused by the challenges posed by a large number of sub-aperture images in complex scenarios. Due to the increasing number of sub-aperture images, it becomes challenging to accurately distinguish between relevant and irrelevant features in a dataset where focused and defocused images are mixed together. Compared with PSPNet-LF and OCR-LF, which implement the direct fusion of sub-aperture images and central-view images, our OAFuser embeds the rich angular feature in an independent branch and focuses on utilizing both spatial and angular features.

Above all, the excellent performance on the UrbanLF-RealE dataset demonstrates the superiority of our design and sets a new record of light field semantic segmentation. The network showcases remarkable accuracy without relying on extensive image preprocessing and additional devices. This validates the applicability of our network in real-world scenarios.

V. ABLATION STUDIES

In this section, we conduct several ablation studies to validate the influence of various modules within our proposed method. The experiments are carried out in Sec. V-A

to thoroughly investigate the effects of diverse components incorporated in our method. Additionally, we conduct several experiments in Sec. V-B to determine the optimal combination in the CARM. Furthermore, we compare the impact of different datasets in Sec. V-C and analyze the per-class performance in Sec. V-D. Moreover, the exploration of the contributions of sub-aperture images is conducted in Sec. V-E.

A. Ablation Study for the Overall Model

Model	#Params(M)	mIoU(%)
OAFuser (ours)	79.2	77.18
- Without CARM	65.0 (-14.2)	75.01 (-2.17)
- SAFM only at Stage One	65.0 (-14.2)	73.50 (-3.68)
- SAFM only at Stage Four	65.0 (-14.2)	73.46 (-3.72)
- Without SAFM	65.0 (-14.2)	73.25 (-3.93)
- Without FFM	58.4 (-20.8)	70.25 (-6.93)

TABLE VI: Ablation study of the OAFuser framework.

As shown in Table VI, we ablate our OAFuser structure gradually. When removing the CARM and replacing it with the Feature Rectification Module (FRM) [13]. The accuracy dramatically decreases by 2.17%. Although the number of parameters is also reduced, our CARM module is essential to overcome challenges such as image mismatching and out-of-focus issues. Besides, we ablate the components of SAFM progressively, *i.e.*, using SAFM in the first or last stage, and without using SAFM. The performances of these three variants are decreased significantly (2~3% drops compared to OAFuser). Especially notably in these variants, the number of parameters remains unchanged, as the angle information is obtained through channel-level feature aggregation with shared weights. This also validates that the introduction of the SAFM efficiently achieves the selection and fusion of rich information from the light field camera, and the network has the capability to handle arbitrary sub-aperture images. Furthermore, we find that the FFM module [13] is also essential since the combination of complementary features is crucial in the multi-modal LF segmentation.

Moreover, we conduct visualization comparisons in this ablation study. Fig. 8 illustrates the difference maps of the cropped region compared to the ground-truth mask, which is generated by the overall OAFuser model, the one without

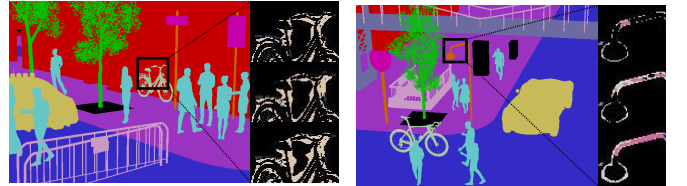


Fig. 8: Visualization of the proposed architecture. From top to bottom are, the entire OAFuser model, OAFuser without CARM, and OAFuser without CARM and SAFM.

Dimension	C	2C	3C	4C	5C
mIoU	70.55	72.87	71.52	71.93	70.57

(a) Exploration of the embedding dimension in Global Rectification. The *Dimension* denotes embedding dimension.

Layers	0	1	2	3	4
mIoU	72.87	73.13	73.06	73.39	71.49

(b) Exploration of Local Rectification.

TABLE VII: Ablation Study of the Central Angular Rectification Module (CARM). *Dimension* denotes the embedding dimension in Global Operation and *Layers* presents the number of 3D convolution within Local Operation. mIoU (%) is reported. The best results are highlighted in red.

CARM, and the other one without CARM and SAFM, respectively. The visualization result indicates the effectiveness of using CARM and SAFM for light-field semantic segmentation.

B. Ablation Study for CARM

To explore the effectiveness of rectifying asymmetric features, we conduct a series of ablation experiments regarding the proposed CARM. As depicted in Table VIIa, we remove the local rectification module and increase the embedding dimension of the global module from C to $4C$ to assess the optimal manner. Subsequently, upon projecting the dimensions to $2C$, our network achieves the highest score of 72.87%. Besides, excessively large dimensions ($>2C$) might hinder the capacity to parse the features. To address the issue, we further explore the number of layers of 3D convolution in Local Rectification, to evaluate the impact. As in Table VIIb, the employment of 3D convolutions proves advantageous for feature rectification when the number of convolutional layers is <4 , and the best mIoU peaks at 73.39%. However, when utilizing four layers of 3D convolutions, the interconnections between different features are disrupted, leading to a diminished mIoU score of 71.49%.

Subsequently, we explore another combination of the Local Rectification Module and Global Rectification Module by parallel addition of features from two groups, which results in a degradation of the discriminative capability of the network.

C. Dataset Comparison

To further prove the performance of our network, we analyze the impact of image quality among distinct datasets. While the number of classes and their distribution exhibits similarity across the datasets, the most prominent difference lies in the image quality, as expounded in UrbanLF [17].

As shown in Fig 9, the presence of noise in out-of-focus images leads to performance degradation for LF-IENet³, LF-IENet⁴, and OCR-LF, resulting in a decline of more than 1% in mIoU. However, the mIoU score of our OAFuser increases by 1.05%. This improvement contributes to the proposed method and the design of our model, which leverage abundant angular information and rectify features from various

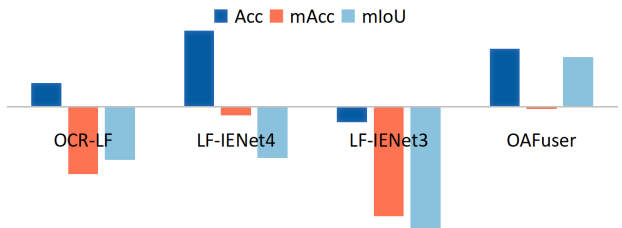


Fig. 9: The performance comparison between different networks. Acc (%), mAcc (%), and mIoU (%) are reported. The best results are highlighted in red.

viewpoints, consequently reducing the impact of image quality on our model. For existing works, the improved accuracy values and decreased mAcc also demonstrate the challenges, which is posed by the decrease in image quality in distinguishing different class boundaries. However, our model, while improving classification accuracy, shows a minimal decrease in mAcc (−0.05%).

D. Per-Class Accuracy Analysis

To comprehensively assess the model’s performance per class and delve deeper into the improvement achieved by our model in comparison with the baseline method, we present a summary of statistical information from different methods in Table VIII. Moreover, the class proportion assisting in data analysis is also introduced.

Given that our baseline method, CMX [13], is designed for two modalities, we first aggregate the sub-aperture images before feeding them into the network. It can be seen that OAFuser significantly outperforms the baseline method across various categories, such as *fence*, *pole*, *sidewalk*, *vehicle*, *bridge* and *rider*, which are crucial for the driving system in urban scenarios. Especially, the recognition capability for *vehicle* even exceeds 97% in IoU.

Those results prove the achievement of our proposed model for segmentation tasks in urban scenes. By incorporating SAFM and CARM, the network unleashes the potential of the angle information from different sub-aperture images and leverages the consistency of variations among sub-aperture images. This enables OAFuser to deliver promising performance.

E. Investigation on the Selection of Sub-Aperture Images

To further prove the contribution of sub-aperture images, several experiments are conducted. As shown in Table IX, compared with our baseline method CMX [13], which is designed for similar modalities fusion, our OAFuser achieves an increase of more than 2% in mIoU. This result further confirms the effectiveness of our design in handling asymmetric data from the light field camera for segmentation tasks.

Dataset	Method	IoU														Acc	mAcc	mIoU
		Bike	Building	Fence	Others	Person	Pole	Road	Sidewalk	Traffic Sign	Vegetation	Vehicle	Bridge	Rider	Sky			
RealE	Proportion	2.27	33.48	3.86	1.59	3.08	1.42	21.36	8.00	0.65	3.05	16.46	2.34	0.24	2.19	n.a.	n.a.	n.a.
	CMX MiT-B4	86.88	90.52	76.27	43.47	91.31	73.47	90.74	68.70	86.22	85.21	96.45	74.33	69.15	96.61	93.00	87.00	80.66
	OAFuser9	87.92	91.95	87.64	48.56	93.63	77.55	91.74	71.92	87.43	89.04	97.05	88.89	79.03	96.61	94.61	89.84	84.93 (+4.55)

TABLE VIII: Per-class statistics of CMX and OAFuser on UrbanLF-RealE dataset are presented. *Proportion* represents the class percentage, and the values are given in percentage (%). The best result is highlighted in red.

Method	mIoU	Improvement
CMX MiT-B0 (RGB V11) [13]	68.40	
OAFuser2 MiT-B0	71.17	+2.77
OAFuser5 MiT-B0	71.92	+3.52
OAFuser9 MiT-B0	72.57	+4.17
OAFuser13 MiT-B0	72.60	+4.20
OAFuser17 MiT-B0	72.87	+4.47
OAFuser21 MiT-B0	72.22	+3.82
OAFuser17 MiT-B4	81.93	+13.53

TABLE IX: Exploration of the contribution of different numbers of sub-aperture images. mIoU (%) is reported. V11 denotes the sub-aperture image from the top-left viewpoint. The best results are highlighted in red.

Furthermore, our network perceives the scene from multiple perspectives, and with the increase of viewpoints, it achieves progressively higher accuracy. This also demonstrates our network's ability to utilize angular information and exhibit the necessity of utilizing more sub-aperture images for segmentation task. OAFuser reaches its peak at OAFuser17.

VI. CONCLUSION

In this paper, we explore the potential of light field cameras for scene understanding with semantic segmentation for autonomous driving and intelligent transportation systems. We propose the Omni-Aperture Fusion (OAFuser) to exploit dense context and angular information from light field apertures. We introduce the Sub-Aperture Fusion Module (SAFM), which enables the network to embed angular information from light field cameras without additional memory costs and ensures the feature consistency of angular features. With the Center Angular Rectification Module (CARM), our network enables the utilization of asymmetric features from different viewpoints. OAFuser sets state-of-art performance compared with existing works on three UrbanLF datasets.

In the future, we strive to establish a new benchmark with more categories and a larger set of training samples to assess the accuracy of using light field cameras for driving scenarios and look into the generalization of OAFuser on more datasets.

REFERENCES

- [1] W. Zhou, S. Dong, J. Lei, and L. Yu, “MTANet: Multitask-aware network with hierarchical multimodal fusion for RGB-T urban scene understanding,” *IEEE Transactions on Intelligent Vehicles*, vol. 8, no. 1, pp. 48–58, 2023.
- [2] J. Fan, F. Wang, H. Chu, X. Hu, Y. Cheng, and B. Gao, “MLFNet: Multi-level fusion network for real-time semantic segmentation of autonomous driving,” *IEEE Transactions on Intelligent Vehicles*, vol. 8, no. 1, pp. 756–767, 2023.
- [3] W. Zhou, Y. Lv, J. Lei, and L. Yu, “Embedded control gate fusion and attention residual learning for RGB-thermal urban scene parsing,” *IEEE Transactions on Intelligent Transportation Systems*, 2023.
- [4] Y. Yang, C. Shan, F. Zhao, W. Liang, and J. Han, “On exploring shape and semantic enhancements for RGB-X semantic segmentation,” *IEEE Transactions on Intelligent Vehicles*, 2023.
- [5] S. Vandenhende, S. Georgoulis, and L. Van Gool, “MTI-Net: Multi-scale task interaction networks for multi-task learning,” in *European Conference on Computer Vision (ECCV)*, vol. 12349, 2020, pp. 527–543.
- [6] M.-H. Guo, C.-Z. Lu, Q. Hou, Z. Liu, M.-M. Cheng, and S.-M. Hu, “SegNeXt: Rethinking convolutional attention design for semantic segmentation,” in *Advances in Neural Information Processing Systems (NeurIPS)*, vol. 35, 2022, pp. 1140–1156.
- [7] I. O. Tolstikhin *et al.*, “MLP-Mixer: An all-MLP architecture for vision,” in *Advances in Neural Information Processing Systems (NeurIPS)*, vol. 34, 2021, pp. 24 261–24 272.
- [8] E. Xie, W. Wang, Z. Yu, A. Anandkumar, J. M. Alvarez, and P. Luo, “SegFormer: Simple and efficient design for semantic segmentation with transformers,” in *Advances in Neural Information Processing Systems (NeurIPS)*, vol. 34, 2021, pp. 12 077–12 090.
- [9] Q. Zhang, Y. Xu, J. Zhang, and D. Tao, “VSA: Learning varied-size window attention in vision transformers,” in *European Conference on Computer Vision (ECCV)*, vol. 13685, 2022, pp. 466–483.
- [10] Z. Zhang, X. Zhang, C. Peng, X. Xue, and J. Sun, “ExFuse: Enhancing feature fusion for semantic segmentation,” in *European Conference on Computer Vision (ECCV)*, vol. 11214, 2018, pp. 273–288.
- [11] R. Zhang, S. A. Candra, K. Vetter, and A. Zakhor, “Sensor fusion for semantic segmentation of urban scenes,” in *2015 IEEE International Conference on Robotics and Automation (ICRA)*, 2015, pp. 1850–1857.
- [12] C. Hazirbas, L. Ma, C. Domokos, and D. Cremers, “FuseNet: Incorporating depth into semantic segmentation via fusion-based CNN architecture,” in *Asian Conference on Computer Vision (ACCV)*, vol. 10111, 2017, pp. 213–228.
- [13] J. Zhang, H. Liu, K. Yang, X. Hu, R. Liu, and R. Stiefelhagen, “CMX: Cross-modal fusion for RGB-X semantic segmentation with transformers,” *IEEE Transactions on Intelligent Transportation Systems*, 2023.
- [14] Y. Wang *et al.*, “Disentangling light fields for super-resolution and disparity estimation,” *IEEE Transactions on Pattern Analysis and Machine Intelligence*, vol. 45, no. 1, pp. 425–443, 2023.
- [15] C. Jia *et al.*, “Semantic segmentation with light field imaging and convolutional neural networks,” *IEEE Transactions on Instrumentation and Measurement*, vol. 70, pp. 1–14, 2021.
- [16] X. Chen *et al.*, “Bi-directional cross-modality feature propagation with separation-and-aggregation gate for RGB-D semantic segmentation,” in *European Conference on Computer Vision (ECCV)*, vol. 12356, 2020, pp. 561–577.
- [17] H. Sheng, R. Cong, D. Yang, R. Chen, S. Wang, and Z. Cui, “UrbanLF: A comprehensive light field dataset for semantic segmentation of urban scenes,” *IEEE Transactions on Circuits and Systems for Video Technology*, vol. 32, no. 11, pp. 7880–7893, 2022.
- [18] T. Leistner, R. Mackowiak, L. Ardizzone, U. Köthe, and C. Rother, “Towards multimodal depth estimation from light fields,” in *2022 IEEE/CVF Conference on Computer Vision and Pattern Recognition (CVPR)*, 2022, pp. 12 943–12 951.
- [19] W. Yan, X. Zhang, H. Chen, C. Ling, and D. Wang, “Light field depth

estimation based on channel attention and edge guidance,” in *2022 China Automation Congress (CAC)*, 2022, pp. 2595–2600.

[20] R. Cong, D. Yang, R. Chen, S. Wang, Z. Cui, and H. Sheng, “Combining implicit-explicit view correlation for light field semantic segmentation,” in *2023 IEEE/CVF Conference on Computer Vision and Pattern Recognition (CVPR)*, 2023, pp. 9172–9181.

[21] J. Zhuang, Z. Wang, and B. Wang, “Video semantic segmentation with distortion-aware feature correction,” *IEEE Transactions on Circuits and Systems for Video Technology*, vol. 31, no. 8, pp. 3128–3139, 2021.

[22] H. Wang, W. Wang, and J. Liu, “Temporal memory attention for video semantic segmentation,” in *2021 IEEE International Conference on Image Processing (ICIP)*, 2021, pp. 2254–2258.

[23] D. G. Dansereau, O. Pizarro, and S. B. Williams, “Decoding, calibration and rectification for lenslet-based plenoptic cameras,” in *2013 IEEE Conference on Computer Vision and Pattern Recognition (CVPR)*, 2013, pp. 1027–1034.

[24] Y. Bok, H.-G. Jeon, and I. S. Kweon, “Geometric calibration of micro-lens-based light field cameras using line features,” *IEEE Transactions on Pattern Analysis and Machine Intelligence*, vol. 39, no. 2, pp. 287–300, 2017.

[25] J. Zhang, K. Yang, A. Constantinescu, K. Peng, K. Müller, and R. Stiefelhagen, “Trans4Trans: Efficient transformer for transparent object and semantic scene segmentation in real-world navigation assistance,” *IEEE Transactions on Intelligent Transportation Systems*, vol. 23, no. 10, pp. 19 173–19 186, 2022.

[26] J. Long, E. Shelhamer, and T. Darrell, “Fully convolutional networks for semantic segmentation,” in *2015 IEEE Conference on Computer Vision and Pattern Recognition (CVPR)*, 2015, pp. 3431–3440.

[27] L.-C. Chen, Y. Zhu, G. Papandreou, F. Schroff, and H. Adam, “Encoder-decoder with atrous separable convolution for semantic image segmentation,” in *European Conference on Computer Vision (ECCV)*, vol. 11211, 2018, pp. 833–851.

[28] V. Badrinarayanan, A. Kendall, and R. Cipolla, “SegNet: A deep convolutional encoder-decoder architecture for image segmentation,” *IEEE Transactions on Pattern Analysis and Machine Intelligence*, vol. 39, no. 12, pp. 2481–2495, 2017.

[29] M. Yang, K. Yu, C. Zhang, Z. Li, and K. Yang, “DenseASPP for semantic segmentation in street scenes,” in *2018 IEEE Conference on Computer Vision and Pattern Recognition (CVPR)*, 2018, pp. 3684–3692.

[30] H. Ding, X. Jiang, B. Shuai, A. Q. Liu, and G. Wang, “Context contrasted feature and gated multi-scale aggregation for scene segmentation,” in *2018 IEEE Conference on Computer Vision and Pattern Recognition (CVPR)*, 2018, pp. 2393–2402.

[31] J. He, Z. Deng, L. Zhou, Y. Wang, and Y. Qiao, “Adaptive pyramid context network for semantic segmentation,” in *2019 IEEE/CVF Conference on Computer Vision and Pattern Recognition (CVPR)*, 2019, pp. 7519–7528.

[32] G. Lin, A. Milan, C. Shen, and I. Reid, “RefineNet: Multi-path refinement networks for high-resolution semantic segmentation,” in *2017 IEEE Conference on Computer Vision and Pattern Recognition (CVPR)*, 2017, pp. 5168–5177.

[33] J. Fu *et al.*, “Dual attention network for scene segmentation,” in *2019 IEEE/CVF Conference on Computer Vision and Pattern Recognition (CVPR)*, 2019, pp. 3146–3154.

[34] W. Wang, T. Zhou, F. Yu, J. Dai, E. Konukoglu, and L. Van Gool, “Exploring cross-image pixel contrast for semantic segmentation,” in *2021 IEEE/CVF International Conference on Computer Vision (ICCV)*, 2021, pp. 7283–7293.

[35] A. Dosovitskiy *et al.*, “An image is worth 16x16 words: Transformers for image recognition at scale,” in *International Conference on Learning Representations (ICLR)*, 2021.

[36] M. Sandler, A. Howard, M. Zhu, A. Zhmoginov, and L.-C. Chen, “MobileNetV2: Inverted residuals and linear bottlenecks,” in *2018 IEEE Conference on Computer Vision and Pattern Recognition (CVPR)*, 2018, pp. 4510–4520.

[37] M. Tan and Q. Le, “EfficientNet: Rethinking model scaling for convolutional neural networks,” in *International Conference on Machine Learning (ICML)*, 2019, pp. 6105–6114.

[38] X. Zhang, X. Zhou, M. Lin, and J. Sun, “ShuffleNet: An extremely efficient convolutional neural network for mobile devices,” in *2018 IEEE Conference on Computer Vision and Pattern Recognition (CVPR)*, 2018, pp. 6848–6856.

[39] X. Hu, K. Yang, L. Fei, and K. Wang, “ACNet: Attention based network to exploit complementary features for RGBD semantic segmentation,” in *2019 IEEE International Conference on Image Processing (ICIP)*, 2019, pp. 1440–1444.

[40] J. Zhang, K. Yang, and R. Stiefelhagen, “Exploring event-driven dynamic context for accident scene segmentation,” *IEEE Transactions on Intelligent Transportation Systems*, vol. 23, no. 3, pp. 2606–2622, 2022.

[41] H. Chen *et al.*, “MMFNet: A multi-modality MRI fusion network for segmentation of nasopharyngeal carcinoma,” *Neurocomputing*, vol. 394, pp. 27–40, 2020.

[42] Z. Xing, L. Yu, L. Wan, T. Han, and L. Zhu, “NestedFormer: Nested modality-aware transformer for brain tumor segmentation,” in *International Conference on Medical Image Computing and Computer-Assisted Intervention (MICCAI)*, 2022, pp. 140–150.

[43] D. Seichter, M. Köhler, B. Lewandowski, T. Wengfeld, and H.-M. Gross, “Efficient RGB-D semantic segmentation for indoor scene analysis,” in *2021 IEEE International Conference on Robotics and Automation (ICRA)*, 2021, pp. 13 525–13 531.

[44] H. Mei *et al.*, “Glass segmentation using intensity and spectral polarization cues,” in *2022 IEEE/CVF Conference on Computer Vision and Pattern Recognition (CVPR)*, 2022, pp. 12 612–12 621.

[45] Y. Sun, W. Zuo, and M. Liu, “RTFNet: RGB-thermal fusion network for semantic segmentation of urban scenes,” *IEEE Robotics and Automation Letters*, vol. 4, no. 3, pp. 2576–2583, 2019.

[46] W. Zhou, J. Liu, J. Lei, L. Yu, and J.-N. Hwang, “GMNet: Graded-feature multilabel-learning network for RGB-thermal urban scene semantic segmentation,” *IEEE Transactions on Image Processing*, vol. 30, pp. 7790–7802, 2021.

[47] Q. Ha, K. Watanabe, T. Karasawa, Y. Ushiku, and T. Harada, “MFNet: Towards real-time semantic segmentation for autonomous vehicles with multi-spectral scenes,” in *2017 IEEE/RSJ International Conference on Intelligent Robots and Systems (IROS)*, 2017, pp. 5108–5115.

[48] J. Zhang *et al.*, “Delivering arbitrary-modal semantic segmentation,” in *2023 IEEE/CVF Conference on Computer Vision and Pattern Recognition (CVPR)*, 2023, pp. 1136–1147.

[49] T. Broedermann, C. Sakaridis, D. Dai, and L. Van Gool, “HRFuser: A multi-resolution sensor fusion architecture for 2D object detection,” in *2023 IEEE International Conference on Intelligent Transportation Systems (ITSC)*, 2023.

[50] A. Wang, M. Wang, X. Li, Z. Mi, and H. Zhou, “A two-stage bayesian integration framework for salient object detection on light field,” *Neural Processing Letters*, vol. 46, pp. 1083–1094, 2017.

[51] J. Zhang, M. Wang, L. Lin, X. Yang, J. Gao, and Y. Rui, “Saliency detection on light field: A multi-cue approach,” *ACM Transactions on Multimedia Computing, Communications, and Applications (TOMM)*, vol. 13, no. 3, pp. 1–22, 2017.

[52] K. Honauer, O. Johannsen, D. Kondermann, and B. Goldluecke, “A dataset and evaluation methodology for depth estimation on 4D light fields,” in *Asian Conference on Computer Vision (ACCV)*, vol. 10113, 2016, pp. 19–34.

[53] J. Peng, Z. Xiong, Y. Wang, Y. Zhang, and D. Liu, “Zero-shot depth estimation from light field using a convolutional neural network,” *IEEE Transactions on Computational Imaging*, vol. 6, pp. 682–696, 2020.

[54] Y. Wang, F. Liu, K. Zhang, G. Hou, Z. Sun, and T. Tan, “LFNet: A novel bidirectional recurrent convolutional neural network for light-field image super-resolution,” *IEEE Transactions on Image Processing*, vol. 27, no. 9, pp. 4274–4286, 2018.

[55] J. Jin, J. Hou, J. Chen, and S. Kwong, “Light field spatial super-resolution via deep combinatorial geometry embedding and structural consistency regularization,” in *2020 IEEE/CVF Conference on Computer Vision and Pattern Recognition (CVPR)*, 2020, pp. 2257–2266.

[56] G. Chen *et al.*, “Fusion-embedding siamese network for light field salient object detection,” *IEEE Transactions on Multimedia*, 2023.

[57] M. Feng, K. Liu, L. Zhang, H. Yu, Y. Wang, and A. Mian, “Learning from pixel-level noisy label: A new perspective for light field saliency detection,” in *2022 IEEE/CVF Conference on Computer Vision and Pattern Recognition (CVPR)*, 2022, pp. 1746–1756.

[58] Y. Wang, L. Wang, J. Yang, W. An, J. Yu, and Y. Guo, “Spatial-angular interaction for light field image super-resolution,” in *European Conference on Computer Vision (ECCV)*, vol. 12368, 2020, pp. 290–308.

[59] Z. Liang, Y. Wang, L. Wang, J. Yang, S. Zhou, and Y. Guo, “Learning non-local spatial-angular correlation for light field image super-resolution,” *arXiv preprint arXiv:2302.08058*, 2023.

[60] S. Zhang, Y. Lin, and H. Sheng, “Residual networks for light field image super-resolution,” in *2019 IEEE/CVF Conference on Computer Vision and Pattern Recognition (CVPR)*, 2019, pp. 11 046–11 055.

[61] S. Zhou, L. Hu, Y. Wang, Z. Sun, K. Zhang, and X.-q. Jiang, “AIF-LFNet: All-in-focus light field super-resolution method considering the depth-varying defocus,” *IEEE Transactions on Circuits and Systems for Video Technology*, 2023.

- [62] G. Wu, Y. Wang, Y. Liu, L. Fang, and T. Chai, “Spatial-angular attention network for light field reconstruction,” *IEEE Transactions on Image Processing*, vol. 30, pp. 8999–9013, 2021.
- [63] H. Zhao, J. Shi, X. Qi, X. Wang, and J. Jia, “Pyramid scene parsing network,” in *2017 IEEE Conference on Computer Vision and Pattern Recognition (CVPR)*, 2017, pp. 6230–6239.
- [64] S. Zheng *et al.*, “Rethinking semantic segmentation from a sequence-to-sequence perspective with transformers,” in *2021 IEEE/CVF Conference on Computer Vision and Pattern Recognition (CVPR)*, 2021, pp. 6881–6890.
- [65] Y. Yuan, X. Chen, and J. Wang, “Object-contextual representations for semantic segmentation,” in *European Conference on Computer Vision (ECCV)*, vol. 12351, 2020, pp. 173–190.
- [66] S. Jain, X. Wang, and J. E. Gonzalez, “Accel: A corrective fusion network for efficient semantic segmentation on video,” in *2019 IEEE/CVF Conference on Computer Vision and Pattern Recognition (CVPR)*, 2019, pp. 8866–8875.
- [67] P. Hu, F. Caba, O. Wang, Z. Lin, S. Sclaroff, and F. Perazzi, “Temporally distributed networks for fast video semantic segmentation,” in *2020 IEEE/CVF Conference on Computer Vision and Pattern Recognition (CVPR)*, 2020, pp. 8815–8824.